

# Quasicrystalline 30° twisted bilayer graphene as an incommensurate superlattice with strong interlayer coupling

Wei Yao<sup>a,b</sup>, Eryin Wang<sup>a,b</sup>, Changhua Bao<sup>a,b</sup>, Yiou Zhang<sup>c</sup>, Kenan Zhang<sup>a,b</sup>, Kejie Bao<sup>c</sup>, Chun Kai Chan<sup>c</sup>, Chaoyu Chen<sup>d</sup>, Jose Avila<sup>d</sup>, Maria C. Asensio<sup>d,e</sup>, Junyi Zhu<sup>c,1</sup>, and Shuyun Zhou<sup>a,b,f,1</sup>

<sup>a</sup>State Key Laboratory of Low Dimensional Quantum Physics, Tsinghua University, Beijing 100084, China; <sup>b</sup>Department of Physics, Tsinghua University, Beijing 100084, China; <sup>c</sup>Department of Physics, The Chinese University of Hong Kong, Hong Kong, China; <sup>d</sup>Synchrotron SOLEIL, L'Orme des Merisiers, Saint Aubin-BP 48, 91192 Gif sur Yvette Cedex, France; <sup>e</sup>Université Paris-Saclay, L'Orme des Merisiers, Saint Aubin-BP 48, 91192 Gif sur Yvette Cedex, France; and <sup>f</sup>Collaborative Innovation Center of Quantum Matter, Beijing 100084, P. R. China

Edited by Hongjie Dai, Department of Chemistry, Stanford University, Stanford, CA, and approved May 25, 2018 (received for review December 1, 2017)

The interlayer coupling can be used to engineer the electronic structure of van der Waals heterostructures (superlattices) to obtain properties that are not possible in a single material. So far research in heterostructures has been focused on commensurate superlattices with a long-ranged Moiré period. Incommensurate heterostructures with rotational symmetry but not translational symmetry (in analogy to quasicrystals) are not only rare in nature, but also the interlayer interaction has often been assumed to be negligible due to the lack of phase coherence. Here we report the successful growth of quasicrystalline 30° twisted bilayer graphene (30°-tBLG), which is stabilized by the Pt(111) substrate, and reveal its electronic structure. The 30°-tBLG is confirmed by low energy electron diffraction and the intervalley double-resonance Raman mode at 1383 cm<sup>-1</sup>. Moreover, the emergence of mirrored Dirac cones inside the Brillouin zone of each graphene layer and a gap opening at the zone boundary suggest that these two graphene layers are coupled via a generalized Umklapp scattering mechanism—that is, scattering of a Dirac cone in one graphene layer by the reciprocal lattice vector of the other graphene layer. Our work highlights the important role of interlayer coupling in incommensurate quasicrystalline superlattices, thereby extending band structure engineering to incommensurate superstructures.

twisted bilayer graphene | NanoARPES | incommensurate heterostructure | band structure engineering | quasicrystalline 30°-tBLG

In van der Waals heterostructures (1), a long-ranged commensurate Moiré superlattice (2–7) forms only when satisfying  $ma_1^{\text{top}} + na_2^{\text{top}} = m'a_1^{\text{bottom}} + n'a_2^{\text{bottom}}$  (8), where  $a_{1,2}^{\text{top}}$  and  $a_{1,2}^{\text{bottom}}$  are primitive lattice vectors for the top and bottom layers, respectively, and  $m, n, m',$  and  $n'$  are integers. Twisted bilayer graphene (tBLG) can be viewed as a simple version of “hetero”-structure, with  $a_{1,2}^{\text{top}}$  rotated by a twisting angle  $\theta_t$  with respect to  $a_{1,2}^{\text{bottom}}$ . In tBLG, commensuration occurs when  $\theta_t$  satisfies (9, 10)

$$\cos \theta_t = \frac{3p^2 + 3pq + q^2/2}{3p^2 + 3pq + q^2}, \quad [1]$$

where  $p$  and  $q$  are two coprime positive integers. Fig. 1A plots the possible twisting angles for forming commensurate tBLG for  $q = 1$ . It is clear that commensuration easily forms around 0°, while for larger twist angles, especially around 30°, incommensurate superlattice is more common (11). In contrast to commensurate superlattice with a long-ranged period (see example in Fig. 1B), incommensurate superlattice lacks a long-ranged translational symmetry in real space while preserving the rotational symmetry; for example, 30°-tBLG (Fig. 1C) is similar to quasicrystals with a classic dodecagonal pattern (12).

Although the electronic structures of commensurate heterostructures have been investigated in recent years (13–17), research on incommensurate heterostructures remains limited for two reasons. On one hand, incommensurate heterostructures are difficult to be stabilized, and thus, they are quite rare under natural growth conditions. On the other hand, it is usually assumed that the interlayer interaction is suppressed due to the lack of phase coherence. For example, incommensurate tBLG has often been taken as a trivial combination of two noninteracting graphene layers (18–20). How the electronic structure is modified in such incommensurate heterostructures, with symmetry analogous to quasicrystalline order, is a fundamental question. Here by growing epitaxial 30°-tBLG successfully on Pt(111) substrate and revealing its electronic structure using angle-resolved photoemission spectroscopy (ARPES) and NanoARPES, we show that the interlayer coupling can modify the electronic structure significantly, leading to mirrored Dirac cones. Additionally, to understand the intriguing stability that is against common belief on bilayer graphene, we performed first-principles calculations and found that such incommensurate 30°-tBLG

## Significance

Interlayer interaction in van der Waals heterostructures could induce many exotic phenomena. Unlike commensurate heterostructures, incommensurate ones have often been neglected, due to the rarity in nature and the assumption of suppressed coherent interlayer movement of electrons. How the interlayer interaction affects the electronic structure of such a nonperiodic heterostructure is a fundamental question. In this work, by successfully growing 30°-twisted bilayer graphene (tBLG) as an example for incommensurate “heterostructure” with quasicrystalline order, we report the emergence of mirrored Dirac cones. We identify that these mirrored Dirac cones are a consequence of the interlayer interaction, showing its importance in the incommensurate structure, which has been overlooked before. These results broaden the application range of van der Waals heterostructure for future electronic devices.

Author contributions: S.Z. designed research; W.Y., E.W., C.B., Y.Z., K.Z., K.B., C.K.C., C.C., J.A., M.C.A., and J.Z. performed research; W.Y. and S.Z. analyzed data; and W.Y., J.Z., and S.Z. wrote the paper.

The authors declare no conflict of interest.

This article is a PNAS Direct Submission.

Published under the PNAS license.

<sup>1</sup>To whom correspondence may be addressed. Email: syzhou@mail.tsinghua.edu.cn or jyzhu@phy.cuhk.edu.hk.

This article contains supporting information online at [www.pnas.org/lookup/suppl/doi:10.1073/pnas.1720865115/-DCSupplemental](http://www.pnas.org/lookup/suppl/doi:10.1073/pnas.1720865115/-DCSupplemental).

Published online June 18, 2018.

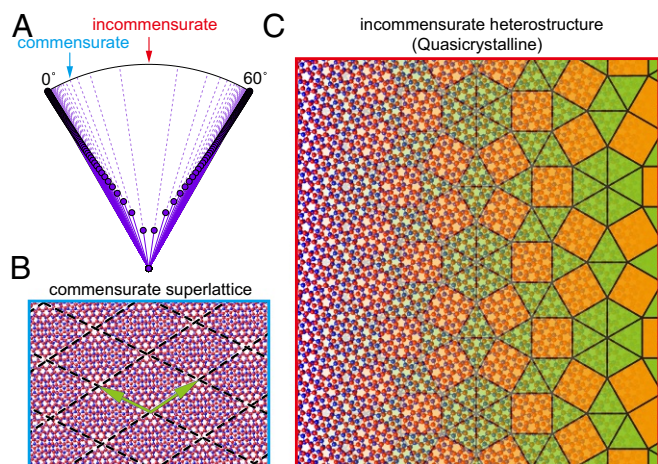


**Fig. 1.** Commensurate and incommensurate tBLG. (A) The distribution of all possible twisting angles  $\theta_t$  for forming commensurate tBLG when  $q = 1$  in Eq. 1. The Moiré period at corresponding twisting angles is represented by the length of the solid line (with logarithmic scale). (B) Commensurate tBLG with 7.34° twisting angle (indicated by the blue arrow in A), showing Moiré pattern with periodic translational symmetry. Green arrows are the Moiré reciprocal lattice vectors. (C) Incommensurate 30°-tBLG without any long-ranged period (indicated by red arrow in A), showing patterns of dodecagonal quasicrystal.

heterostructure is stabilized under appropriate substrate conditions.

## Results

**Growth of 30°-tBLG.** The 30°-tBLG sample was grown on the Pt(111) substrate by carbon segregation from the bulk substrate (21, 22). Fig. 2A shows the low energy electron diffraction (LEED) of bottom monolayer graphene at 30° azimuthal orientation (blue arrow) relative to the substrate. Our previous

work shows that distinguished from other graphene/Pt with commensurate (e.g.,  $2 \times 2$ ,  $3 \times 3$ ) Moiré superstructures (21), the interface between the 30° monolayer graphene and the Pt(111) substrate is incommensurate without forming any Moiré pattern, leading to nearly free-standing monolayer graphene (22). Further increasing the annealing temperature and time can lead to a thicker graphene sample with a new set of diffraction peaks emerging at 0° orientation (red arrow in Fig. 2B) coexisting with those at 30°, and such a graphene sample is the focus of the current work. The lattice constants extracted from LEED show that there is negligible strain ( $<0.2\%$ ; see *SI Appendix, Fig. S1* for details) between the 30° and 0° graphene layers, and the absence of additional reconstructed diffraction spots in the LEED pattern further supports that they do not form commensurate superlattice. If these diffraction peaks come from the same graphene domains, this would imply that 0° graphene is stacked on top of the bottom 30° graphene layer—namely, a 30°-tBLG is formed. In the following, we will provide direct experimental evidence for the conjectured incommensurate 30°-tBLG from Raman spectroscopy and reveal its electronic structure from ARPES measurements.

**Intervalley Double-Resonance (DR) Raman Mode.** Raman spectroscopy is a powerful tool for characterizing the vibrational mode in graphene (23) and can provide direct information about the sample thickness and stacking. Fig. 2G shows a typical optical image of the as-grown sample. The optical image shows strong intensity contrast, with a darker region of  $\approx 10 \mu\text{m}$  overlapping with the brighter region. The Raman spectra in Fig. 2C show stronger intensity for the darker region (red curve) than the brighter region (blue curve), suggesting that the darker region is thicker. The spectra for both regions show characteristic features of monolayer graphene (23), in which the 2D mode shows a single Lorentzian peak with stronger intensity than the G mode. This suggests that the top and bottom flakes are both monolayer graphene, and the thicker region is not a Bernal (AB stacking) bilayer graphene but is rather a bilayer graphene with a

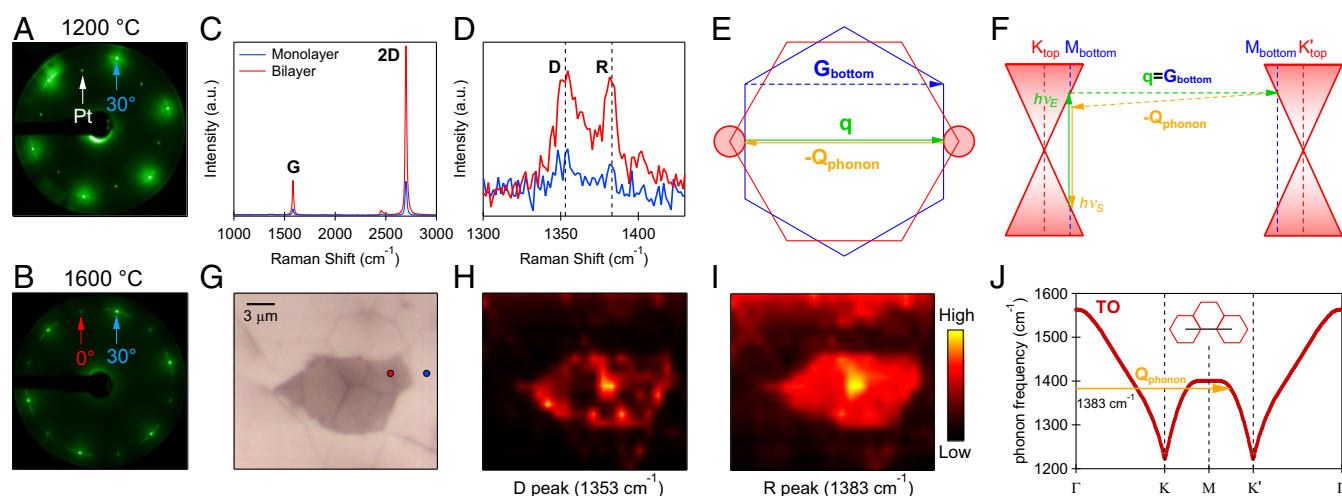


**Fig. 2.** Observation of DR Raman mode in 30°-tBLG. (A) The LEED pattern for the graphene sample after annealing at 1,200 °C measured at electron beam energy of 135 eV. (B) The LEED pattern for the graphene sample at the higher annealing temperature of 1,600 °C. (C) Measured Raman spectrum for monolayer and bilayer region, respectively, covering the range of G peak and the 2D peak. (D) Zoom in of C for a range from 1,300 to 1,430 cm<sup>-1</sup>. (E) The geometry for electron momentum transferring in the DR Raman process of the observed R mode. (F) The schematic drawing for the DR process of R mode in graphene band structure (not in scale). An electron at one Dirac cone from the top layer is photo-excited to the conduction band, scattered by one reciprocal lattice vector of the bottom layer  $\mathbf{q} = \mathbf{G}_{\text{bottom}}$ , and subsequently scattered back by phonon with vector  $\mathbf{Q}_{\text{phonon}}$ . (G) The optical image for the measured area. The red and blue dots indicate the measuring positions of spectra in C and D. (H) The Raman map for the D peak, integrating intensity from 1,343 to 1,363 cm<sup>-1</sup>. (Scale bar: 3 μm.) (I) The Raman map for the R peak, integrating intensity from 1,373 to 1,393 cm<sup>-1</sup>. (Scale bar: 3 μm.) (J) The phonon spectrum of the TO mode along high symmetric direction, taken from ref. 26. The arrow indicates the momentum of transferring R mode phonon. Inset shows the high-symmetry path in  $k$ -space for the phonon spectrum. The left hexagon is the first Brillouin zone (BZ).

large twisting angle instead (24). More importantly, when zooming in the spectra between 1,300 and 1,430  $\text{cm}^{-1}$ , the bilayer region shows two peaks centered at 1,353  $\text{cm}^{-1}$  and 1,383  $\text{cm}^{-1}$ , respectively (Fig. 2D). The peak at 1,353  $\text{cm}^{-1}$  is the D mode of graphene, which is caused by the limited size or defects (23). The Raman mapping for this peak (Fig. 2H) shows that it only appears at the edges of the bilayer region or defect centers, consistent with the nature of the D peak. In contrast, the peak at 1,383  $\text{cm}^{-1}$  (“R” peak) is observed in the whole bilayer graphene region (Fig. 2I), indicating that it is intrinsic to the tBLG.

Since the energy of the R mode is close to that of the D mode, the R mode likely has a similar origin as the D mode: intervalley DR Raman process (25, 26). The key process for the intervalley DR Raman process involves a special scattering process (by defect, phonon, or Moiré pattern) in which photoexcited electrons at one valley are scattered to another valley by a nonzero momentum transfer  $\mathbf{q}$  and subsequently decay back to the original valley by emitting a phonon with wave vector  $\mathbf{Q}_{\text{phonon}} = \mathbf{q}$  (see Fig. 2F). While D mode is induced by defect scattering between two neighboring Dirac cones, instead we claim that the R mode in our case is caused by scattering between two opposite Dirac cones that are connected by one reciprocal lattice vector of the bottom graphene layer with  $\mathbf{q} = \mathbf{G}_{\text{bottom}}$  (see Fig. 2E and F). This is verified by observing a phonon mode with matching momentum and energy in the transverse optical (TO) phonon spectrum along the  $\Gamma$ -K-M-K'- $\Gamma$  direction (see Fig. 2I). The phonon momentum of the R mode is not a Moiré reciprocal vector of any commensurate superlattice, suggesting that the bilayer region is an incommensurate  $30^\circ$ -tBLG. It also reveals an unreported scattering process involving the reciprocal lattice vector of the bottom layer in this interesting  $30^\circ$ -tBLG region. This novel scattering process for the observed R mode is closely related to the interlayer interaction to be discussed below and is supported by the exotic electronic structure of the  $30^\circ$ -tBLG, which we will investigate next.

**Observation of Mirrored Dirac Cone.** The electronic structure of the sample was first measured by conventional ARPES with a beam size of  $\sim 100 \mu\text{m}$ . Fig. 3A shows the ARPES intensity map at  $-0.8 \text{ eV}$ . Characteristic conical contours appear at the K points of the graphene Brillouin zone (BZ) for both  $0^\circ$  and  $30^\circ$  layers (labeled as  $K_{0^\circ}$  and  $K_{30^\circ}$ ), in agreement with the coexistence of  $0^\circ$ - and  $30^\circ$ -graphene layers observed in the LEED pattern. Additional contours with weaker intensity are detected inside the first BZ near  $K_{0^\circ}$  (green arrows in Fig. 3B) when enhancing the weak features using the logarithmic scale. The curvature images (Fig. 3C) at different energies with higher visibility show that these contours expand from low to high binding energy similar to the Dirac cones at  $K_{0^\circ}$ , and they occur at the reflected position of  $K_{0^\circ}$  (indicated by a green arrow and labeled as  $K_R$ ) with respect to the  $30^\circ$  BZ edges (blue lines). The dispersion near the  $K_R$  also shows linear behavior, which is the reflected image of the Dirac cone at  $K_{0^\circ}$  (Fig. 3D). The mirrored Dirac cone shows similar intensity asymmetry caused by the dipole matrix element (27), with stronger intensity between  $K_{0^\circ}$  ( $K_R$ ) and the M point of the  $30^\circ$ -graphene layer  $M_{30^\circ}$ , suggesting that it comes from the original Dirac cone at the opposite momentum valley and is strongly related to the transfer mechanism discussed above for the DR Raman mode (more details are shown in Discussion). Moreover, the suppression of intensity at the crossing point  $M_{30^\circ}$  between the original and mirrored Dirac cones indicates a gap opening (pointed by black arrows in Fig. 3D). Such mirrored Dirac cones and gap opening are not observed in the bottom monolayer  $30^\circ$ -graphene (see SI Appendix for details). Furthermore, the gap happens to appear at the BZ boundary of the bottom layer and is away from the substrate bands (see SI Appendix for details), suggesting

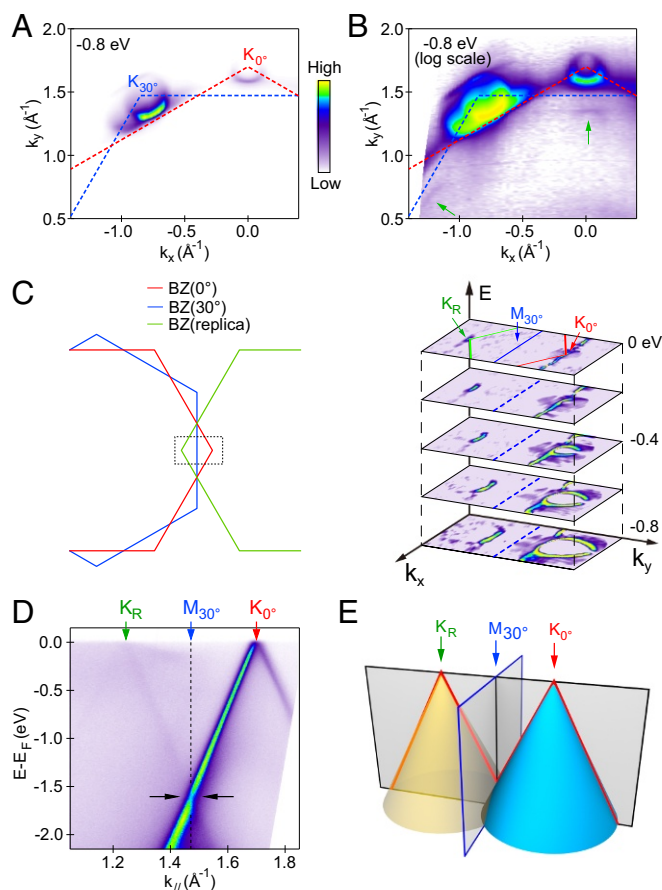


**Fig. 3.** Observation of mirrored Dirac cone in  $30^\circ$ -tBLG. (A) Intensity map at  $-0.8 \text{ eV}$ . The BZs of  $0^\circ$ -graphene and  $30^\circ$ -graphene are indicated by the dashed lines. (B) The same map as A but with the logarithmic scale. Green arrows indicate the traces of replica Dirac cones. (C) Schematic drawing of the BZ (Left) and the 2D curvature image of constant energy maps for the region marked by the rectangle at energies from  $E_F$  to  $-0.8 \text{ eV}$  (Right). The BZ boundary of  $0^\circ$ ,  $30^\circ$ , and replica bands are shown as red, blue, and green lines. (D) The measured Dirac-type dispersion near the K point of the  $0^\circ$  orientation. The three vertical arrows indicate the K point of  $0^\circ$ -graphene, the M point of  $30^\circ$ -graphene, and the K point of the replica BZ. The gap is indicated by the horizontal arrows. (E) Schematic illustration showing the mirrored relation between the original and the emerging replica Dirac cone.

that they are caused not by the graphene-substrate interaction but by intrinsic properties of the  $30^\circ$ -tBLG. Therefore, our ARPES results confirm that the  $30^\circ$  graphene layer spatially overlaps with the  $0^\circ$  graphene layer and they interact with each other.

**The Band Structures with Spatial Resolution.** The electronic structure of  $30^\circ$ -tBLG is further confirmed by NanoARPES (28), which is capable of resolving the electronic band structure of coexisting graphene structures with spatial resolution at the  $\approx 120 \text{ nm}$  scale. A spatially resolved intensity map is shown in Fig. 4A, where we can distinguish different regions and map out their distinct electronic structure. Region labeled by B shows dispersion along the  $\Gamma$ -M direction of the  $30^\circ$  bottom graphene layer (Fig. 4B), while region C shows dispersions from the  $30^\circ$ -tBLG, with dispersion along the  $\Gamma$ -K direction of the  $0^\circ$  top graphene layer coexisting with that along the  $\Gamma$ -M direction of the bottom  $30^\circ$  graphene layer (Fig. 4C). Therefore, dispersions measured by NanoARPES with spatial resolution provide definitive experimental evidence for the  $30^\circ$ -tBLG, and the mirrored Dirac cones indeed originate from this newly discovered tBLG



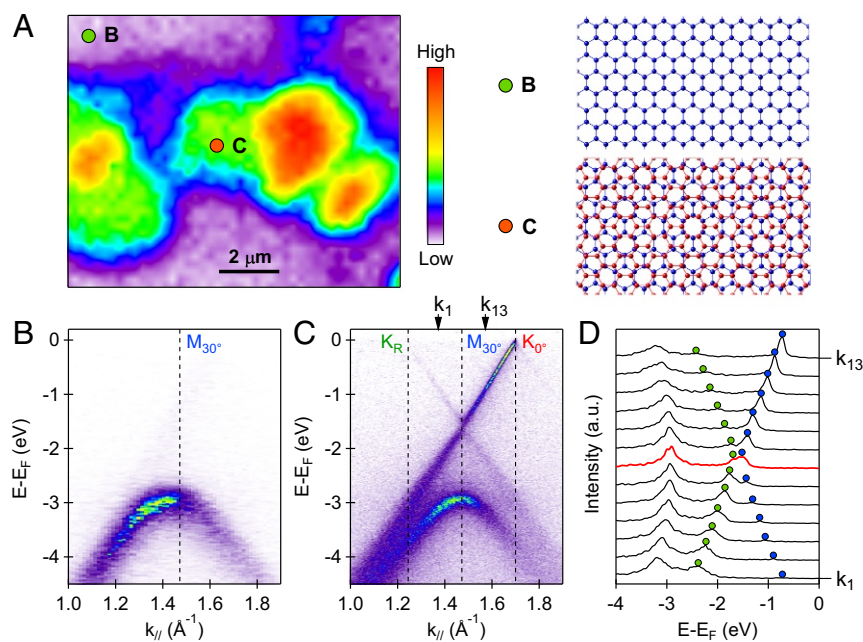


**Fig. 4.** Confirmation of 30°-tBLG and the electronic structure by NanoARPES measurements. (A) Spatial intensity map obtained by integrating the energy from -1.5 eV to E<sub>F</sub>. The structures for regions B and C are schematically shown on *Right*. (B and C) Dispersion cuts taken at regions marked by B and C in A. (D) The energy distribution curves (EDCs) taken in the momentum range marked by the arrows in C. The EDC through the cross point of the original and mirrored bands is shown by the red color. Blue and green circles mark the peak positions.

structure. Moreover, by focusing only in the 30°-tBLG region, sharper dispersions can be obtained, and the gap at the M point becomes more obvious. Analysis from the EDCs for 30°-tBLG (Fig. 4D) shows a gap at the M<sub>30°</sub> point, suggesting the Dirac cone at K<sub>0°</sub> and the mirrored Dirac cone are hybridized.

**Band Gap in *k* Space.** To track the evolution of the gap at the crossing points between the original Dirac cone at K<sub>0°</sub> and the mirrored Dirac cone at K<sub>R</sub>, we show in Fig. 5A dispersions measured from cuts 1 to 5 (labeled in Fig. 5B). The gap size is quantified by the peak separation of the EDCs at the crossing

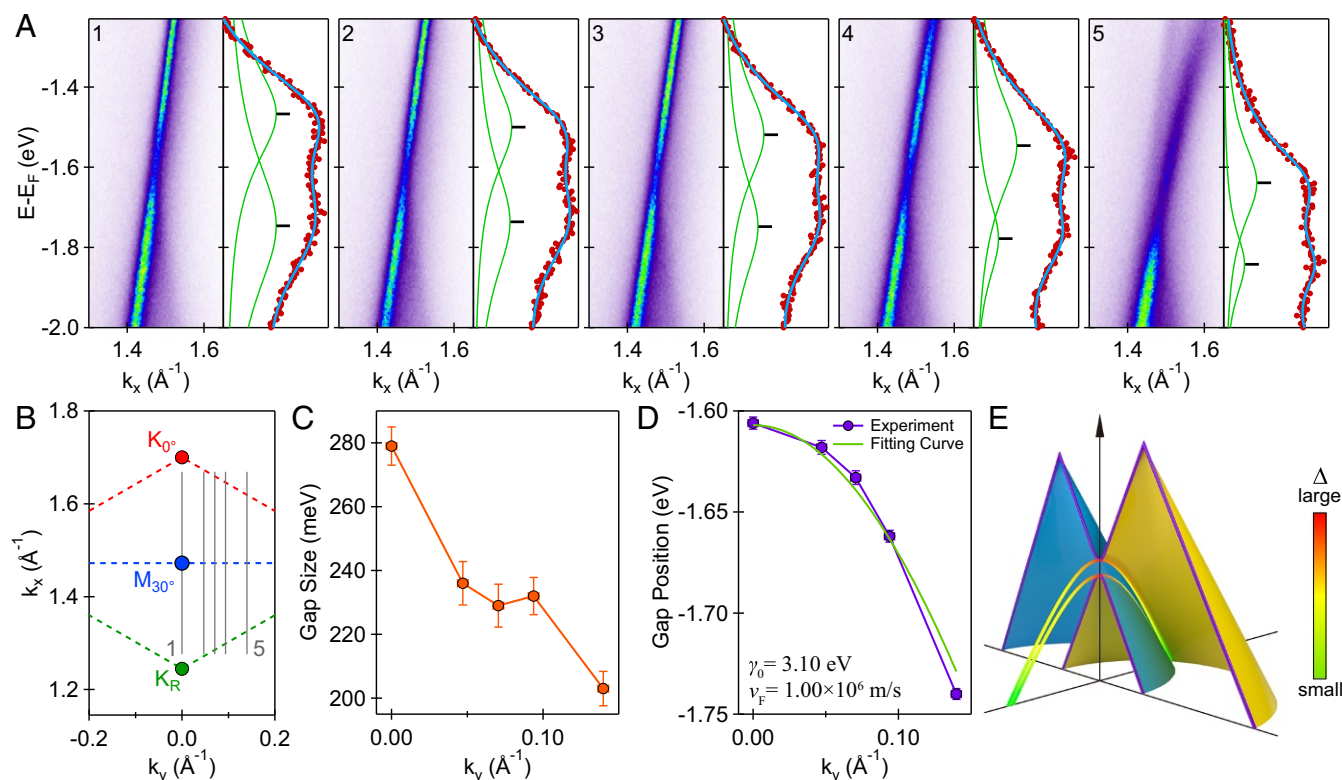


**Fig. 5.** Evolution of gap size and gap position in *k* space. (A) Five different cuts located at different positions in the *k* space shown in B. The EDCs crossing the gap are shown on the right of the spectrum as red symbols. The fitting curves are plotted as blue lines, and green curves are the two Lorentzian peaks from fitting results. Black markers show the positions of the two peaks. (B) Schematic BZ showing the positions of the five cuts in A. (C) The gap size along the *k<sub>y</sub>* direction. (D) The gap position along the *k<sub>y</sub>* direction. The green line is the fitting curve by the tight-binding model. (E) Cartoon diagram for the two Dirac cones and their intersecting line with a gap. The color indicates the gap size.

points, and the extracted value is plotted in Fig. 5C. It is clear that the gap size decreases from the maximum value of  $\sim 280$  meV at the  $M_{30^\circ}$  point to  $\sim 200$  meV when deviating from the  $M_{30^\circ}$  point. In addition, we can define the gap position as the average of the two peak positions. The gap position curve in Fig. 5D shows that the gap is located at the intersecting line of the two Dirac cones; hence, it is possible to fit the gap positions by the energy dispersion obtained from a tight-binding model (see *SI Appendix* for details). The fitting curve (green curve in Fig. 5D) is in good agreement with the experimental data, giving a nearest neighbor hopping parameter  $\gamma_0$  of 3.10 eV, which is closed to the value derived from theoretical calculations (29). The Fermi velocity  $v_F = \sqrt{3}a\gamma_0/2$  ( $a \sim 2.46$  Å) is extracted to be  $1.003 \pm 0.002 \times 10^6$  m/s. A schematic summary of the gap between the original and mirrored Dirac cones is shown in Fig. 5E.

**Theoretical Calculation.** Ab initio calculations are performed to reveal the electronic structure of  $30^\circ$ -tBLG and investigate the stability. Since Bloch theorem does not apply to the nonperiodic structure and an infinitely large cell is beyond the calculation capability, a finite supercell of  $(5 \times 5)/(3\sqrt{3} \times 3\sqrt{3})R30^\circ$  is constructed to mimic the nonperiodic  $30^\circ$ -tBLG system. The calculated electronic structure in Fig. 6A shows the band gap opening at the M point of the counterpart layer, with the gap value close to the experimental measurements. An interesting observation regards the stability of  $30^\circ$ -tBLG when the Pt substrate is included in the calculation. While the formation energy of free-standing  $30^\circ$ -tBLG is 1.6 meV/(C atom) higher than the more common AB-stacking BLG, inclusion of the substrate leads to formation energy of 4.1 meV/(C atom) lower than AB-stacking one, which explains why  $30^\circ$ -tBLG emerges in our sample and suggests an important role of the Pt substrate in stabilizing the  $30^\circ$ -tBLG. By investigating real-space projection of the Bloch states, a significant coupling between the carbon p orbital and platinum d orbital (shown in Fig. 6B) is revealed near Fermi level. Since such p-d coupling occurs

at the  $\Gamma$  point, and phase matching between graphene and the Pt substrate is less critical (due to zero  $k$ -vector). Therefore, it could thus exist in systems with weak and incoherent sample-substrate interaction such as our sample, contributing positively to the stability of grown  $30^\circ$ -tBLG on the Pt substrate. Extrapolating to a larger supercell, like  $5 \times 5$ ,  $7 \times 7$ , and  $16 \times 16$ , the stability of  $30^\circ$ -tBLG is further enhanced (see *SI Appendix* for details), and the electronic structure remains similar, suggesting that the calculation conclusion mentioned above still holds at the limit of an infinitely large cell or the incommensurate structure. Our calculation, although not perfect, still provides some theoretical insights into the physics and stability of the  $30^\circ$ -tBLG.

## Discussion

Unlike the satellite Dirac cones appearing in the commensurate graphene system with long-ranged Moiré pattern (30–32), the emergence of mirrored Dirac cones in incommensurate  $30^\circ$ -tBLG indicates an unusual scattering mechanism in this structure. Based on a generalized Umklapp scattering process (33), we build up a tight-binding model with second-order perturbation further included (see *SI Appendix* for details) and reveal a general coupling condition for two Bloch states in one layer of the twisted bilayer system:

$$\mathbf{k}_1^u = \mathbf{k}_2^u - \mathbf{G}^u + \mathbf{G}^d \quad [2]$$

where  $\mathbf{k}_1^u$  and  $\mathbf{k}_2^u$  are wave vectors of the two Bloch states in one layer, and  $\mathbf{G}^u$  and  $\mathbf{G}^d$  are the reciprocal lattice vectors of the same layer and its counterpart, respectively. Applying this condition, we propose a scattering mechanism for electrons in  $30^\circ$ -tBLG: Dirac cone at the  $K'$  point of one graphene layer  $K'_{0^\circ}$  is scattered by one reciprocal lattice vector of the other layer  $\mathbf{G}_{30^\circ}$ , forming a mirrored Dirac cone  $K_R$  near the opposite momentum valley at  $K_{0^\circ}$  as schematically shown in Fig. 6C. This corresponds to the simplest case in Eq. 2 for  $\mathbf{G}^u = \mathbf{0}$  and  $\mathbf{G}^d = \mathbf{G}_{30^\circ}$ . Such a mechanism is confirmed by three experimental observations. First of all, the momentum of the mirrored Dirac point  $K_R$  is connected to the other graphene valley  $K'_{0^\circ}$  by just one reciprocal lattice vector of the other  $30^\circ$  layer  $\mathbf{G}_{30^\circ}$ . Second, the asymmetry of the intensity contour for the mirrored Dirac cone is identical to the one at  $K'$  (see Fig. 3D or Fig. 4C), suggesting that the mirrored Dirac cone is scattered from the  $K'$  point. Third, such a scattering mechanism is fully consistent with the observed R mode in Raman spectrum. Not only for the incommensurate structure, this scattering mechanism is also able to account for the appearance of replica Dirac cones in those commensurate graphene systems following the same analysis (33). Thus, this mechanism can be applied to other van der Waals heterostructures beyond tBLG.

## Conclusions

In summary, we have successfully grown  $30^\circ$ -tBLG, a typical example for incommensurate superlattice with quasicrystalline order. The realization of  $30^\circ$ -tBLG provides opportunities for investigating the intriguing physics of quasicrystalline superlattice. Moreover, by revealing the mirrored Dirac cones in a  $30^\circ$ -tBLG, we provide direct experimental evidence for the strong interlayer coupling through a coherent scattering process in such an incommensurate superlattice. Such a scattering mechanism can be applied to engineer the band structure of both commensurate and incommensurate tBLG as well as other van der Waals heterostructures.

## Materials and Methods

**Sample Growth.** The graphene sample was obtained by annealing one Pt(111) substrate to about  $1,600^\circ\text{C}$ . At this high temperature, the carbon

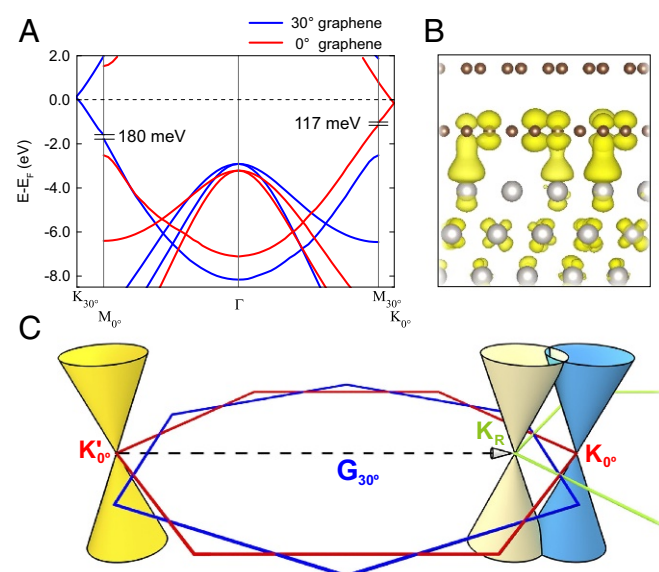


**Fig. 6.** Electronic structure of  $30^\circ$ -tBLG from first-principles calculations. (A) Band structure of a  $(5 \times 5)/(3\sqrt{3} \times 3\sqrt{3})R30^\circ$ -tBLG in the extended zone scheme. The energy gap of  $\pi$ -band at the M point of the other layer is indicated. (B) Real-space projection of the Bloch state at  $\Gamma$  point near the Fermi level, showing a clear bonding state between  $p_z$  orbital of C (brown balls) and  $d$  orbital of Pt (white balls). (C) Schematic illustration for the band structure of  $30^\circ$ -tBLG, showing the emergence of mirrored Dirac cones.

impurities would segregate from the bulk to the surface, forming graphene film.

**ARPES and NanoARPES.** Conventional ARPES measurements were performed at the home laboratory with a Helium discharge lamp and beamline 10.0.1 of Advanced Light Source (ALS) with synchrotron radiation source. The NanoARPES measurements were performed at the analysis nano-spot angle-resolved photoemission spectroscopy (ANTARES) endstation of Synchrotron SOLEIL, in France, with a lateral spatial resolution of 120 nm. The sample temperature was kept at 20 K for measurements at ALS and 40 K for those at SOLEIL.

**Calculations.** The calculations were based on VASP code (34, 35) with plane wave basis set (36, 37). We adopted opt86b-vdW functional (38, 39) to include the van der Waals interactions. A periodic  $(5 \times 5)$  on the  $(3\sqrt{3} \times 3\sqrt{3})R30^\circ$  structure was created to simulate the  $30^\circ$ -tBLG because it is impossible to directly simulate the very large nonperiodic bilayer. The lower layer is slightly compressed about 1.8% to fit the Pt lattice, and the upper layer is slightly stretched about 2% to partially compensate for

the compression from the lower layer. Extensive convergence tests have been performed in terms of vacuum, film thickness, and k-point sampling. Although our calculations were based on one periodic structure, such effects would be extrapolated to nonperiodic structures of  $30^\circ$ -tBLG.

**ACKNOWLEDGMENTS.** This work is supported by Ministry of Science and Technology of China Grants 2016YFA0303004 and 2015CB921001, National Natural Science Foundation of China Grants 11334006 and 11725418, Science Challenge Project 20164500122, and Beijing Advanced Innovation Center for Future Chip (ICFC). The theoretical work is supported by the General Research Fund (Grant 2130490) from Research Grants Council in Hong Kong. The Synchrotron SOLEIL is supported by the Center National de la Recherche Scientifique (CNRS) and the Commissariat à l'Energie Atomique et aux Energies Alternatives (CEA), France. This work is supported by a public grant overseen by the French National Research Agency (ANR) as part of the "Investissements d'Avenir" program (Labex NanoSaclay, reference ANR-10-LABX-0035) as well as the French Ministre des affaires étrangères et européennes (MAEE), the Center National de la Recherche Scientifique (CNRS) through Information and Communication Technology (ICT)-ASIA Program Grant 3226/DGM/ATT/RECH.

- Geim AK, Grigorieva IV (2013) Van der Waals heterostructures. *Nature* 499:419–425.
- Dean CR, et al. (2010) Boron nitride substrates for high-quality graphene electronics. *Nat Nano* 5:722–726.
- Xue J, et al. (2011) Scanning tunnelling microscopy and spectroscopy of ultra-flat graphene on hexagonal boron nitride. *Nat Mater* 10:282–285.
- Dean CR, et al. (2013) Hofstadter's butterfly and the fractal quantum Hall effect in Moiré superlattices. *Nature* 497:598–602.
- Hunt B, et al. (2013) Massive Dirac fermions and Hofstadter butterfly in a van der Waals heterostructure. *Science* 340:1427–1430.
- Yu GL, et al. (2014) Hierarchy of Hofstadter states and replica quantum Hall ferromagnetism in graphene superlattices. *Nat Phys* 10:525–529.
- Wang E, et al. (2016) Gaps induced by inversion symmetry breaking and second-generation Dirac cones in graphene/hexagonal boron nitride. *Nat Phys* 12:1111–1115.
- Moon P, Koshino M (2012) Energy spectrum and quantum Hall effect in twisted bilayer graphene. *Phys Rev B* 85:195458.
- Mele EJ (2010) Commensuration and interlayer coherence in twisted bilayer graphene. *Phys Rev B* 81:161405(R).
- dos Santos JMBL, Peres NMR, Neto AHC (2012) Continuum model of the twisted graphene bilayer. *Phys Rev B* 86:155449.
- Woods CR, et al. (2014) Commensurate-incommensurate transition in graphene on hexagonal boron nitride. *Nat Phys* 10:451–456.
- Koren E, Duerig U (2016) Superlubricity in quasicrystalline twisted bilayer graphene. *Phys Rev B* 93:201404(R).
- Li G, et al. (2010) Observation of van Hove singularities in twisted graphene layers. *Nat Phys* 6:109–113.
- Luican A, et al. (2011) Single-layer behavior and its breakdown in twisted graphene layers. *Phys Rev Lett* 106:126802.
- Ohta T, et al. (2012) Evidence for interlayer coupling and Moiré periodic potentials in twisted bilayer graphene. *Phys Rev Lett* 109:186807.
- Kandyba V, Yablonskikh M, Barinov A (2015) Spectroscopic characterization of charge carrier anisotropic motion in twisted few-layer graphene. *Sci Rep* 5:16388.
- Razado-Colambo I, et al. (2016) NanoARPES of twisted bilayer graphene on SiC: Absence of velocity renormalization for small angles. *Sci Rep* 6:27261.
- Sprinkle M, et al. (2009) First direct observation of a nearly ideal graphene band structure. *Phys Rev Lett* 103:226803.
- Hass J, et al. (2008) Why multilayer graphene on 4H-SiC(0001) behaves like a single sheet of graphene. *Phys Rev Lett* 100:125504.
- Kim Y, et al. (2013) Breakdown of the interlayer coherence in twisted bilayer graphene. *Phys Rev Lett* 110:096602.
- Sutter P, Sadowski JT, Sutter E (2009) Graphene on Pt(111): Growth and substrate interaction. *Phys Rev B* 80:245411.
- Yao W, et al. (2015) Monolayer charge-neutral graphene on platinum with extremely weak electron-phonon coupling. *Phys Rev B* 92:115421.
- Ferrari AC, et al. (2006) Raman spectrum of graphene and graphene layers. *Phys Rev Lett* 97:187401.
- Kim K, et al. (2012) Raman spectroscopy study of rotated double-layer graphene: Misorientation-angle dependence of electronic structure. *Phys Rev Lett* 108:246103.
- Thomsen C, Reich S (2000) Double resonant Raman scattering in graphite. *Phys Rev Lett* 85:5214–5216.
- Carozo V, et al. (2011) Interlayer interaction in general incommensurate atomic layers. *Nano Lett* 11:4527–4534.
- Shirley EL, Terminello L, Santoni A, Himpel F (1995) Brillouin-zone-selection effects in graphite photoelectron angular distributions. *Phys Rev B* 51:13614.
- Bostwick A, Rotenberg E, Avila J, Asensio MC (2012) Zooming in on electronic structure: NanoARPES at SOLEIL and ALS. *Synchrotron Radiat News* 25:19–25.
- Wallace PR (1947) The band theory of graphite. *Phys Rev* 71:622–634.
- Pletikoscic I, et al. (2009) Dirac cones and minigaps for graphene on Ir(111). *Phys Rev Lett* 102:056808.
- Starodub E, et al. (2011) In-plane orientation effects on the electronic structure, stability, and Raman scattering of monolayer graphene on Ir(111). *Phys Rev B* 83:125428.
- Wang E, et al. (2016) Gaps induced by inversion symmetry breaking and second-generation Dirac cones in graphene/hexagonal boron nitride. *Nat Phys* 12:1111–1115.
- Koshino M (2015) Interlayer interaction in general incommensurate atomic layers. *New J Phys* 17:015014.
- Kresse G, Hafner J (1994) Ab initio molecular-dynamics simulation of the liquid-metal-amorphous-semiconductor transition in germanium. *Phys Rev B* 49:14251.
- Kresse G, Furthmüller J (1996) Efficiency of ab-initio total energy calculations for metals and semiconductors using a plane-wave basis set. *Comput Mater Sci* 6:15–50.
- Blöchl PE (1994) Projector augmented-wave method. *Phys Rev B* 50:17953.
- Kresse G, Joubert D (1999) From ultrasoft pseudopotentials to the projector augmented-wave method. *Phys Rev B* 59:1758–1775.
- Lee K, Murray ED, Kong L, Lundqvist BI, Langreth DC (2010) Higher-accuracy van der Waals density functional. *Phys Rev B* 82:081101(R).
- Klimeš J, Bowler DR, Michaelides A (2011) Van der Waals density functionals applied to solids. *Phys Rev B* 83:195131.